



Numerical simulation of infragravity waves in fringing reefs using a shock-capturing non-hydrostatic model



Gangfeng Ma ^{a,*}, Shih-Feng Su ^b, Shuguang Liu ^c, Jyh-Cheng Chu ^d

^a Department of Civil and Environmental Engineering, Old Dominion University, Norfolk, VA, USA

^b Department of Water Resources and Environmental Engineering, Tamkang University, Taipei, Taiwan

^c Department of Hydraulic Engineering, Tongji University, Shanghai, China

^d Harbor and Coastal Engineering Department, CECI Engineering Consults, Inc., Taipei, Taiwan

ARTICLE INFO

Article history:

Received 17 January 2014

Accepted 26 April 2014

Available online 13 May 2014

Keywords:

Infragravity waves

Non-hydrostatic model

Fringing reefs

Taiping Island

ABSTRACT

The shock-capturing non-hydrostatic model NHWAVE is used to study infragravity wave processes in the fringing reefs. The reef effects on the water column are modeled by using a drag force formulation. The model is calibrated and validated against flume observations in two laboratory experiments, which have different reef platforms. In both experiments, the model is shown to be capable of well predicting wave height, wave setup as well as energy density spectrum evolution at the reef flat. The results demonstrate that NHWAVE can be used to model wave processes in the reefs, including wave breaking and nonlinear wave dynamics. The model is finally applied to examine the effects of coral degradation on infragravity wave motions in the Taiping island, which is a fringing reef island in the South China Sea. It is found that the infragravity wave motions at the reef flat on the western island are possibly related to the fundamental mode of resonance. The coral degradation may greatly increase the infragravity wave energy at the reef flat. It would also lead to energy transfer to the lower-frequency waves, generating longer-period waves in the reef flat.

Published by Elsevier Ltd.

1. Introduction

Coral reefs are widely distributed in the tropical regions of the Pacific, Indian, and Atlantic Oceans, and provide habitat for a wide variety of marine species. The general reef platforms can be divided into three morphological zones: the forereef (or reef slope), which normally has a steep slope; the reef flat, which has a broad, horizontal, shallow and rough bottom extending to the island beach; and the reef edge, which connects the reef slope and the reef flat. As offshore waves propagate onshore to a reef platform, they initially break near the reef edge, and then continuously dissipate energy while passing through the shallow reef flat due to reef-induced friction. Numerous studies have demonstrated that up to 70–95% of wave energy can be dissipated during propagation onto the beach (Hardy and Young, 1996; Lowe et al., 2005; Massel and Gourlay, 2000). In this sense, coral reefs protect coastal areas from wave action. However, coastal damages have occasionally been reported along the low-lying reef coasts during typhoons (Nakaza and Hino, 1991). These damages are postulated to be caused by infragravity wave oscillations (Nwogu and Demirbilek, 2010). Infragravity waves may also affect sediment dynamics in the

surf zone (Bowen and Huntley, 1984). Therefore, it is critical to study infragravity wave processes in the reef environment, which requires the development of sophisticated predictive models.

The generation mechanisms of infragravity waves have been extensively studied since the first report of low frequency motions on the sandy beach (Munk and Sargent, 1948). Longuet-Higgins and Stewart (1962, 1964) proposed that bound infragravity waves can be generated by groups of short waves through spatial gradients in radiation stress. Symonds et al. (1982) suggested that the temporal variation of the breaking position introduced by incident wave groups of varying amplitudes would lead to the generation of free long waves propagating both offshore and onshore within the surf zone. Later, nonlinear triad interactions accounting for energy transfer among the spectral peaks towards higher frequencies and lower frequencies were developed (Battjes et al., 2004; Herbers et al., 1994; Herbers and Guza, 1994; Janssen et al., 2003) and applied to explain infragravity waves observed in the field and laboratory experiments.

Although the platforms of sandy beaches and fringing reefs are physically different, the generation of infragravity waves on reefs is similar to that on sandy coasts. Both field and laboratory measurements have shown that the infragravity wave frequencies (typically 0.005–0.05 Hz) dominate the energy spectrum at the fringing reef flats (Brander et al., 2004; Hardy and Young, 1996; Young, 1989). These low-frequency motions are closely related to

* Corresponding author. Tel.: +1 757 683 4732.

E-mail address: gma@odu.edu (G. Ma).

the fundamental mode of resonance at the flat (Lugo-Fernández et al., 1998; Nakaza and Hino, 1991; Péquignet et al., 2009). To understand these processes, various numerical models have been developed recently. For instance, Sheremet et al. (2011) applied both phase-resolving and phase-averaged wave models based on the extended nonlinear mild-slope equation to simulate swell, sea and infragravity waves in a laboratory fringing reef. After comparing with the measurements of Demirbilek et al. (2007), it was shown that the performance of the phase-resolving model was better than that of the phase-averaged model. Nwogu and Demirbilek (2010) developed a nonlinear Boussinesq equation model to investigate infragravity wave motions over the fringing reefs. Model results were verified against the laboratory data of Demirbilek et al. (2007) and showed a good agreement in wave height distributions as well as infragravity oscillations at the reef flat. Roeber and Cheung (2012) utilized a shock-capturing Boussinesq-type model to fringing reefs in both laboratory experiments and field environment in Hawaii. Their model well reproduced the development of infragravity waves. Although successful applications of Boussinesq equation models on reef environments have been reported, one major concern with these types of models is the relatively steep reef slope, which may violate the underlying bottom-slope assumption of weakly dispersive models (Nwogu and Demirbilek, 2010). Pomeroy et al. (2012) used the numerical model XBeach based on the wave action equation to predict infragravity waves in a field-scale fringing reef. The model results revealed that infragravity waves at the reef flat are dominantly shoreward propagating. The seaward propagating infragravity waves reflected from the shoreline were small due to the significant energy dissipation over the wide and hydraulically rough flat. This was further confirmed by Van Dongeren et al. (2013).

Except the above-mentioned models, the non-hydrostatic models introduced recently have shown great potential for resolving wave dynamics in the surf zone, including wave breaking (Zijlema and Stelling, 2008; Ma et al., 2012; Smit et al., 2013), nonlinear wave dynamics (Smit et al., 2014) as well as infragravity wave motions in sandy beaches (Rijnsdorp et al., 2014). Compared to the Boussinesq equation models, non-hydrostatic models are capable of simulating highly dispersive fully nonlinear wave processes, thus can be applied to steep slope environments. In addition, the shock-capturing numerical scheme recently introduced into the non-hydrostatic model (Ma et al., 2012) is capable of capturing wave breaking without relying on empirical formulations. In this study, we will show the capabilities of NHWAVE (Ma et al., 2012) in simulating infragravity waves in the fringing reefs. The reef effects on the water column are modeled by a drag force formulation. The model will be validated by laboratory measurements of wave heights as well as wave spectra in the reefs.

The remainder of the paper is organized as follows. In Section 2, the governing equations of NHWAVE are presented. The shock-capturing numerical schemes and boundary conditions are given in Section 3. In Section 4, the model is validated by the measurements in two laboratory experiments. In Section 5, the model is applied to study infragravity wave processes in Taiping Island, which is a fringing reef island in the South China Sea. Finally, the paper is concluded in Section 6.

2. Governing equations

NHWAVE (Ma et al., 2012) is a three-dimensional non-hydrostatic wave model that is capable of predicting instantaneous free surface and 3D flow structures. The model has been used to study tsunami wave generation by submarine landslides (Ma et al., 2013a) and wave damping by vegetation canopies (Ma et al.,

2013b). It is based on the assumption that the free surface is a single value function of horizontal coordinates. Thus, the computational domain is bounded by the free surface $z = \eta(x, y)$ and the bottom $z = -h(x, y)$. The governing equations of NHWAVE are the incompressible Navier–Stokes equations in well-balanced conservative form, formulated in time-dependent surface and terrain-following σ coordinate, which is defined as

$$t = t^*, \quad x = x^*, \quad y = y^*, \quad \sigma = \frac{z^* + h}{D} \quad (1)$$

where the total water depth $D(x, y, t) = h(x, y) + \eta(x, y, t)$.

With σ coordinate transformation, the well-balanced mass and momentum equations are given by

$$\frac{\partial D}{\partial t} + \frac{\partial Du}{\partial x} + \frac{\partial Dv}{\partial y} + \frac{\partial \omega}{\partial \sigma} = 0 \quad (2)$$

$$\frac{\partial \mathbf{U}}{\partial t} + \frac{\partial \mathbf{F}}{\partial x} + \frac{\partial \mathbf{G}}{\partial y} + \frac{\partial \mathbf{H}}{\partial \sigma} = \mathbf{S}_h + \mathbf{S}_p + \mathbf{S}_\tau + \mathbf{S}_c \quad (3)$$

where $\mathbf{U} = (Du, Dv, Dw)^T$. The fluxes are

$$\mathbf{F} = \begin{pmatrix} Duu + \frac{1}{2}g\eta^2 + gh\eta \\ Duv \\ Duw \end{pmatrix}, \quad \mathbf{G} = \begin{pmatrix} Duv \\ Dvv + \frac{1}{2}g\eta^2 + gh\eta \\ Dvw \end{pmatrix}, \quad \mathbf{H} = \begin{pmatrix} u\omega \\ v\omega \\ w\omega \end{pmatrix}$$

The first three source terms on the right-hand side of Eq. (3) account for the contributions from hydrostatic pressure, non-hydrostatic pressure and turbulent diffusion, given by

$$\mathbf{S}_h = \begin{pmatrix} g\eta\frac{\partial h}{\partial x} \\ g\eta\frac{\partial h}{\partial y} \\ 0 \end{pmatrix}, \quad \mathbf{S}_p = \begin{pmatrix} -\frac{D}{\rho}\left(\frac{\partial p}{\partial x} + \frac{\partial p}{\partial \sigma}\frac{\partial \sigma}{\partial x}\right) \\ -\frac{D}{\rho}\left(\frac{\partial p}{\partial y} + \frac{\partial p}{\partial \sigma}\frac{\partial \sigma}{\partial y}\right) \\ -\frac{1}{\rho}\frac{\partial p}{\partial \sigma} \end{pmatrix}, \quad \mathbf{S}_\tau = \begin{pmatrix} DS_{\tau_x} \\ DS_{\tau_y} \\ DS_{\tau_z} \end{pmatrix}$$

where $DS_{\tau_x}, DS_{\tau_y}, DS_{\tau_z}$ are diffusion terms. In this paper, we focus on wave propagation in the absence of strongly sheared currents, in which the effects of turbulence on the wave motion are marginal and can be neglected (Rijnsdorp et al., 2014). Therefore, the diffusion terms are omitted in the following simulations. The fourth term \mathbf{S}_c accounts for the effects of coral reef on the water column. In a hydrodynamic sense, a coral reef is a complex array of obstacles that exerts a drag force on water moving over the reef (Rosman and Hench, 2011). The traditional approach to parameterize this drag is to increase the bottom friction coefficient (Lowe et al., 2009; Nwogu and Demirbilek, 2010), which is typically one order of magnitude larger than that over the bed without reefs. Following this approach, we model the drag force exerted by the coral reef on the water column as

$$\mathbf{S}_c = DF_c = \frac{1}{2}C_f|\mathbf{u}|\mathbf{u} \quad (4)$$

in which F_c is the drag force, C_f is the drag coefficient and $\mathbf{u} = (u, v, w)$ is the velocity vector. The drag coefficient will be calibrated using the laboratory measurements in the following sections.

In the above formulations, ω is the vertical velocity in the σ coordinate image domain, given by

$$\omega = D\left(\frac{\partial \sigma}{\partial t^*} + u\frac{\partial \sigma}{\partial x^*} + v\frac{\partial \sigma}{\partial y^*} + w\frac{\partial \sigma}{\partial z^*}\right) \quad (5)$$

with

$$\begin{aligned} \frac{\partial \sigma}{\partial t^*} &= -\frac{\sigma}{D}\frac{\partial D}{\partial t} \\ \frac{\partial \sigma}{\partial x^*} &= \frac{1}{D}\frac{\partial h}{\partial x} - \frac{\sigma}{D}\frac{\partial D}{\partial x} \\ \frac{\partial \sigma}{\partial y^*} &= \frac{1}{D}\frac{\partial h}{\partial y} - \frac{\sigma}{D}\frac{\partial D}{\partial y} \\ \frac{\partial \sigma}{\partial z^*} &= \frac{1}{D} \end{aligned} \quad (6)$$

To solve the water depth D , we integrate the continuity Eq. (2) from $\sigma=0$ to 1. By using the boundary conditions at the bottom and surface for ω , we may obtain the equation for free surface movement:

$$\frac{\partial D}{\partial t} + \frac{\partial}{\partial x} \left(D \int_0^1 u \, d\sigma \right) + \frac{\partial}{\partial y} \left(D \int_0^1 v \, d\sigma \right) = 0 \quad (7)$$

3. Numerical schemes and boundary conditions

The well-balanced continuity and momentum Eqs. (2) and (3) are discretized by a combined finite-volume and finite-difference approach with a second-order Godunov-type scheme. Following the numerical framework of NHWAVE (Ma et al., 2012), the velocities are defined at the cell centers, while the pressure is defined at the vertically facing cell faces in order to accurately prescribe zero pressure condition at the free surface. The two-stage second-order nonlinear Strong Stability-Preserving (SSP) Runge–Kutta scheme (Gottlieb et al., 2001) is adopted for time stepping in order to obtain second-order temporal accuracy. At the first stage, an intermediate quantity $\mathbf{U}^{(1)}$ is evaluated using a typical first-order, two-step projection method given by

$$\frac{\mathbf{U}^* - \mathbf{U}^n}{\Delta t} = - \left(\frac{\partial \mathbf{F}}{\partial x} + \frac{\partial \mathbf{G}}{\partial y} + \frac{\partial \mathbf{H}}{\partial \sigma} \right)^n + \mathbf{S}_h^n + \mathbf{S}_c^n \quad (8)$$

$$\frac{\mathbf{U}^{(1)} - \mathbf{U}^*}{\Delta t} = \mathbf{S}_p^{(1)} \quad (9)$$

where \mathbf{U}^n represents the \mathbf{U} value at time level n , \mathbf{U}^* is the intermediate value in the two-step projection method, and $\mathbf{U}^{(1)}$ is the final first stage estimate.

At the second stage, the velocity field is updated to a second intermediate level using the same projection method, after which the Runge–Kutta algorithm is used to obtain a final value of the solution at the $n+1$ time level:

$$\frac{\mathbf{U}^* - \mathbf{U}^{(1)}}{\Delta t} = - \left(\frac{\partial \mathbf{F}}{\partial x} + \frac{\partial \mathbf{G}}{\partial y} + \frac{\partial \mathbf{H}}{\partial \sigma} \right)^{(1)} + \mathbf{S}_h^{(1)} + \mathbf{S}_c^{(1)} \quad (10)$$

$$\frac{\mathbf{U}^{(2)} - \mathbf{U}^*}{\Delta t} = \mathbf{S}_p^{(2)} \quad (11)$$

$$\mathbf{U}^{n+1} = \frac{1}{2} \mathbf{U}^n + \frac{1}{2} \mathbf{U}^{(2)} \quad (12)$$

To solve Eqs. (8) and (10), the shock-capturing HLL approximate Riemann solver (Harten et al., 1983) is applied to estimate fluxes at the cell faces. In the HLL TVD scheme, the values of the conservative variables within a cell are calculated using a reconstruction method based on the cell center data (Zhou et al., 2001). Usually a piecewise linear reconstruction is used, leading to a second order scheme. For \mathbf{U} in the cell i , we have

$$\mathbf{U} = \mathbf{U}_i + (x - x_i) \Delta \mathbf{U}_i \quad (13)$$

where $\Delta \mathbf{U}_i$ is the gradient of \mathbf{U} , which is calculated by

$$\Delta \mathbf{U}_i = \text{avg} \left(\frac{\mathbf{U}_{i+1} - \mathbf{U}_i}{x_{i+1} - x_i}, \frac{\mathbf{U}_i - \mathbf{U}_{i-1}}{x_i - x_{i-1}} \right) \quad (14)$$

in which avg is a slope limiter which is used to avoid spurious oscillations in the reconstruction data at the cell faces. In this study, the van Leer limiter is adopted, which is given by

$$\text{avg}(a, b) = \frac{a|b| + |a|b}{|a| + |b|} \quad (15)$$

The left and right values of \mathbf{U} at cell face $(i+\frac{1}{2})$ are given by

$$\mathbf{U}_{i+\frac{1}{2}}^L = \mathbf{U}_i + \frac{1}{2} \Delta x_i \Delta \mathbf{U}_i, \quad \mathbf{U}_{i+\frac{1}{2}}^R = \mathbf{U}_{i+1} - \frac{1}{2} \Delta x_{i+1} \Delta \mathbf{U}_{i+1} \quad (16)$$

The flux $\mathbf{F}(\mathbf{U}^L, \mathbf{U}^R)$ is calculated by solving a local Riemann problem at each horizontally facing cell face. In the present study, the HLL Riemann solver is employed. The flux at the cell interface $(i+\frac{1}{2})$ is determined by

$$\mathbf{F}(\mathbf{U}^L, \mathbf{U}^R) = \begin{cases} \mathbf{F}(\mathbf{U}^L) & \text{if } s_L \geq 0 \\ \mathbf{F}^*(\mathbf{U}^L, \mathbf{U}^R) & \text{if } s_L < 0 < s_R \\ \mathbf{F}(\mathbf{U}^R) & \text{if } s_R \leq 0 \end{cases} \quad (17)$$

where

$$\mathbf{F}^*(\mathbf{U}^L, \mathbf{U}^R) = \frac{s_R \mathbf{F}(\mathbf{U}^L) - s_L \mathbf{F}(\mathbf{U}^R) + s_L s_R (\mathbf{U}^R - \mathbf{U}^L)}{s_R - s_L} \quad (18)$$

with wave speeds s_L and s_R defined by

$$s_L = \min(u^L - \sqrt{gD_L}, u_s - \sqrt{gD_s}) \quad (19)$$

$$s_R = \max(u^R + \sqrt{gD_R}, u_s + \sqrt{gD_s}) \quad (20)$$

where u_s and $\sqrt{gD_s}$ are estimated by

$$u_s = \frac{1}{2} (u^L + u^R) + \sqrt{gD_L} - \sqrt{gD_R} \quad (21)$$

$$\sqrt{gD_s} = \frac{\sqrt{gD_L} + \sqrt{gD_R}}{2} + \frac{u^L - u^R}{4} \quad (22)$$

The fluxes at cell faces in y and z directions are calculated in a similar manner. To close the two-stage SSP computation, the non-hydrostatic pressure has to be solved at each stage. The non-hydrostatic pressure is obtained by solving the Poisson equation, which is given by (Ma et al., 2012)

$$\begin{aligned} \frac{\partial}{\partial x} \left[\frac{\partial p}{\partial x} + \frac{\partial p}{\partial \sigma} \frac{\partial \sigma}{\partial x} \right] + \frac{\partial}{\partial y} \left[\frac{\partial p}{\partial y} + \frac{\partial p}{\partial \sigma} \frac{\partial \sigma}{\partial y} \right] + \frac{\partial}{\partial \sigma} \left(\frac{\partial p}{\partial x} \right) \frac{\partial \sigma}{\partial x} \\ + \frac{\partial}{\partial \sigma} \left(\frac{\partial p}{\partial y} \right) \frac{\partial \sigma}{\partial y} + \left[\left(\frac{\partial \sigma}{\partial x} \right)^2 + \left(\frac{\partial \sigma}{\partial y} \right)^2 + \frac{1}{D^2} \right] \frac{\partial}{\partial \sigma} \left(\frac{\partial p}{\partial \sigma} \right) \\ = \frac{\rho}{\Delta t} \left(\frac{\partial u^*}{\partial x} + \frac{\partial u^*}{\partial \sigma} \frac{\partial \sigma}{\partial x} + \frac{\partial v^*}{\partial y} + \frac{\partial v^*}{\partial \sigma} \frac{\partial \sigma}{\partial y} + \frac{1}{D} \frac{\partial w^*}{\partial \sigma} \right) \end{aligned} \quad (23)$$

The above equation is discretized by a second-order space-centered finite difference method and solved by a preconditioned GMRES solver using the high performance preconditioner HYPRE software library (<http://acts.nersc.gov/hypre>).

The surface elevation is obtained by solving continuity Eq. (7) explicitly. The time step Δt is adaptive during the simulation, following the Courant–Friedrichs–Lowy (CFL) criterion

$$\Delta t = C \min \left[\min \frac{\Delta x}{|u_{i,j,k}| + \sqrt{gD_{i,j}}}, \min \frac{\Delta y}{|v_{i,j,k}| + \sqrt{gD_{i,j}}}, \min \frac{\Delta \sigma D_{i,j}}{|w_{i,j,k}|} \right] \quad (24)$$

where C is the Courant number, which is taken as 0.5 to ensure accuracy and stability in the current model.

To solve the equations, boundary conditions are required for all the physical boundaries. At the free surface, we have

$$\frac{\partial u}{\partial \sigma} \Big|_{\sigma=1} = \frac{\partial v}{\partial \sigma} \Big|_{\sigma=1} = 0, \quad w|_{\sigma=1} = \frac{\partial \eta}{\partial t} + u \frac{\partial \eta}{\partial x} + v \frac{\partial \eta}{\partial y} \quad (25)$$

The dynamic pressure is zero at the free surface.

At the bottom, the normal velocity w is imposed through the kinematic boundary condition:

$$w|_{\sigma=0} = -u \frac{\partial h}{\partial x} - v \frac{\partial h}{\partial y} \quad (26)$$

This paper is focused on wave propagation in the absence of strongly sheared currents. The effects of turbulence on wave motion are neglected. Therefore, free-slip boundary condition is

used for horizontal velocities at the bottom:

$$\frac{\partial u}{\partial \sigma} \Big|_{\sigma=0} = \frac{\partial v}{\partial \sigma} \Big|_{\sigma=0} = 0 \quad (27)$$

The dynamics pressure has zero gradient at the bottom.

At the closed boundaries or vertical walls, free-slip boundary conditions are imposed. The normal velocity and the tangential stress are set to zero. The normal pressure gradient is zero. At inflow, both free surface and velocities are specified. To facilitate the parallel implementation, we used two ghost cells at each boundaries. The boundary conditions are specified at the ghost cells.

4. Modeling infragravity waves in laboratory fringing reefs

In this section, the model is used to reproduce the data collected in a series of laboratory experiments, which were conducted under the Surge and Wave Island Modeling Studies (SWIMS) Program. One experiment was conducted at the Engineer Research and Development Center (ERDC), and the other was conducted at University of Michigan (UM).

4.1. ERDC experiments

The ERDC experiments were conducted in a 45.7 m long, 0.91 m wide and 0.91 m deep 2D wave flume to measure wave transformation, setup, and runup on a generalized reef. The reef was constructed of 2-in thick acrylic glass, which was router cut to form a surface based on bathymetry of the Guam reef. A series of tests were performed with two forereef slopes, 1:2.5 and 1:5. Irregular waves were generated based on a TMA spectral shape for peak frequencies between 0.35 and 1.0 Hz (7–20 s, prototype) and significant wave heights up to 17.7 cm (8.8 m, prototype), under various water levels.

In the numerical simulation, we chose the reef topography with forereef slope of 1:5. The computational domain and the reef topography are shown in Fig. 1. The domain is 20 m long, which is discretized by 1000 horizontal grids with $\Delta x = 0.02$ m. Three vertical layers are selected, which has been proved to be sufficient to capture the wave dispersion characteristics (Ma et al., 2012). The model is used to reproduce two experimental runs. One has the incident irregular waves with significant wave height of $H_s = 0.0749$ m, peak wave period of $T_p = 1.41$ s and water depth of $h = 0.439$ m. The other has the incident irregular waves with significant wave height of $H_s = 0.1567$ m, peak wave period of $T_p = 1.84$ s and water depth of $h = 0.490$ m. The incident waves are generated by specifying analytical solutions of free surface elevation as well as flow velocities at the left boundary. The numerical results are recorded at 12 wave gauges as shown in Fig. 1.

Fig. 2 presents the model-data comparisons of cross-shore distributions of significant wave height, infragravity wave height and wave setup using three different drag coefficients: $C_f = 0.1, 0.2$, 0.3 at the reef flat. The significant wave height is calculated based on Rayleigh wave height distribution $H_s = 4\sigma_\eta$, where σ_η is the

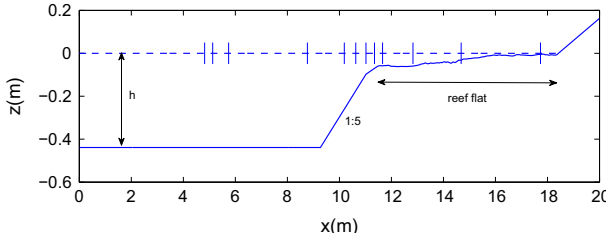


Fig. 1. The computational domain and reef topography. The solid lines show the locations of 12 wave gauges (gauges 1–12 from left to right).

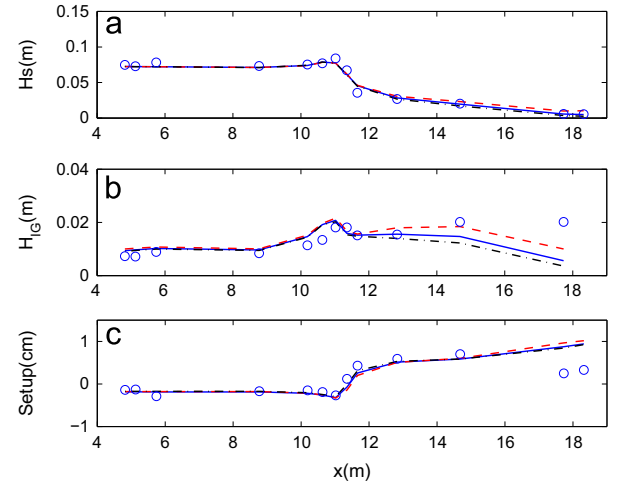


Fig. 2. Model-data comparisons of cross-shore distributions of (a) spectral significant wave height, (b) infragravity wave height and (c) setup with different reef drag coefficients C_f in the reef flat for case 1 (incident wave conditions: $H_{mo} = 0.0749$ m, $T_p = 1.41$ s, $h = 0.439$ m). Circles: measurements; solid lines: $C_f = 0.2$; dashed lines: $C_f = 0.1$; dash-dotted lines: $C_f = 0.3$.

standard deviation of free surface. The infragravity wave height is estimated from the wave spectra at wave gauges $H_{IG} = 4\sqrt{\int_{f_c}^{f_p} s(f) df}$, where $f_c = 0.5f_p$ demarcates the infragravity wave band and the gravity wave band, f_p is the peak frequency. As we can see, the significant wave height and wave setup are not sensitive to the drag coefficient, possibly because the reef flat in the laboratory experiment is narrow. To assess the model's accuracy quantitatively, we compute the model skill as (Reniers et al., 2006)

$$Skill = 1 - \sqrt{\frac{\frac{1}{N} \sum_{n=1}^N (X_p - X_o)^2}{\frac{1}{N} \sum_{n=1}^N X_o^2}} \quad (28)$$

where N is the total number of observations and X is the considered quantity with subscript p and subscript o denoting the predicted and observed values respectively. The simulated wave heights agree well with the measurements. The model skills of predicting significant wave heights with $C_f = 0.1, 0.2$ and 0.3 are 0.922, 0.931 and 0.928, respectively. On the other hand, the infragravity wave height in the reef flat is quite sensitive to the drag coefficient. With decreasing drag coefficient, the infragravity wave height increases. The agreement between the measurements and simulations is better with the drag coefficient of $C_f = 0.1$. The model results also indicate that the reef induced drag force plays a significant role in long-period wave motions in the reef flat. As far as the model calibration is concerned, the drag coefficient of $C_f = 0.1$ produces better results. Therefore, we choose $C_f = 0.1$ in the following simulations.

From Fig. 2, we also find that the location of wave breaking ($x = 11.0$ m) is well captured by the model without taking into account the turbulence effects. This is consistent with the numerical models of Bradford (2011) and Zijlema and Stelling (2008), who successfully simulated breaking waves with Euler equations. This result indicates that the shock-capturing scheme employed in the model is able to well describe the initiation of wave breaking process and the associated energy losses, as well as the shock propagation of broken waves in the reef flat. In Fig. 2, we see that the wave breaking occurs at the reef edge, where it has the maximum wave set-down of 2.7 mm. The simulated wave setup matches fairly well with the measurement, except gauges 12 and

13. The reason for the sudden drop of wave setup at these two gauges is unclear.

Fig. 3 compares the simulated and measured energy density spectra at gauges 4, 6, 8 and 11. It can be seen from **Fig. 1** that gauge 4 is located at the deep water region, gauge 6 is located at the reef slope, gauge 8 is situated at the reef edge and gauge 11 is in the middle of the reef flat. From the evolution of wave spectrum at these four gauges, we can clearly see the energy transfer from the high-frequency waves to the low-frequency waves. In the offshore, the wave spectrum has a shape of JONSWAP spectrum. The model underpredicts the spectral density at high frequency band. The reason is possibly because the incident wave spectrum follows JONSWAP spectrum in the simulation, while it is a TMA spectrum in the experiment. Despite this discrepancy, the model well predicts the spectral density near the peak frequency and the low-frequency band. In the reef slope, due to nonlinear wave-wave interactions, high-frequency wave energy is slowly transferred to low-frequency waves, leading to the generation of infragravity waves. In the inner reef flat (gauge 11), the wave energy is mostly concentrated in the infragravity wave band. From **Fig. 3**, we see that the model-data comparisons are fairly good, indicating that the model is capable of capturing these nonlinear wave processes in the reef environment.

The detailed comparisons of measured and calculated energy density are shown in **Fig. 4**. In the gravity wave band, the distributions of spectral density are well simulated by the model, except that the spectral density at high frequency ($f \geq 1.5$ Hz) is underestimated by the model similar to the finding in **Fig. 3**. At the reef edge, the spectral density in the gravity wave band decreases dramatically due to the wave energy dissipation by breaking, accompanied by an increase of the spectral density in the infragravity wave band. The infragravity wave energy is concentrated at the frequency of around $f=0.1$ Hz. The model well captures the generation of infragravity wave energy at the reef edge. In the reef flat, the wave energy is gradually transferred to lower frequency waves. In the measurements, the maximum infragravity wave energy density is found at the shoreline centered at the frequency of 0.04 Hz. However, the simulated infragravity wave energy density reaches its maximum value in the central reef flat and

decays onshore. The discrepancy is likely to be caused by overestimation of reef drag in the inner reef flat, where the water depth is very shallow.

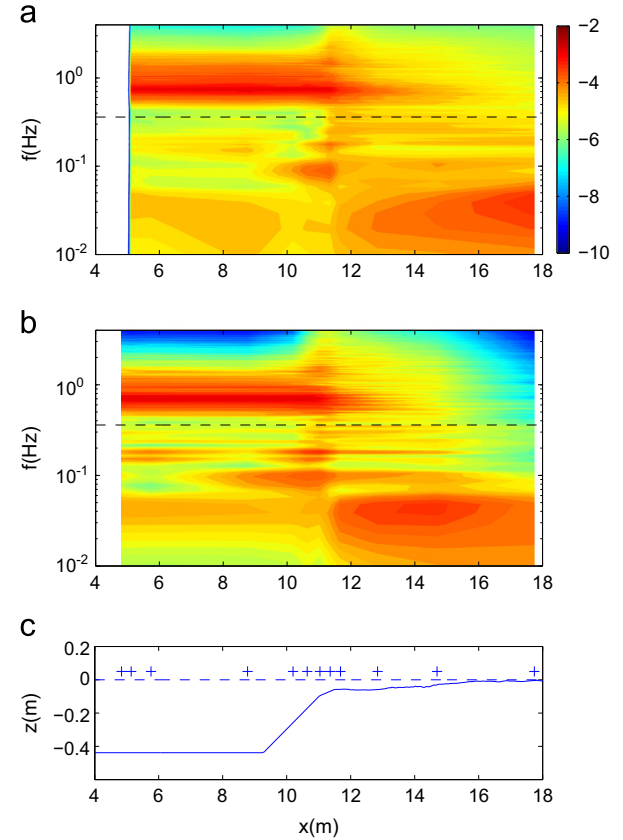


Fig. 4. Comparisons of measured (panel (a)) and simulated (panel (b)) energy density distributions for case 1 (incident wave conditions: $H_{mo}=0.0749$ m, $T_p=1.41$ s, $h=0.439$ m). The dashed lines demarcate the gravity wave band and infragravity wave band.

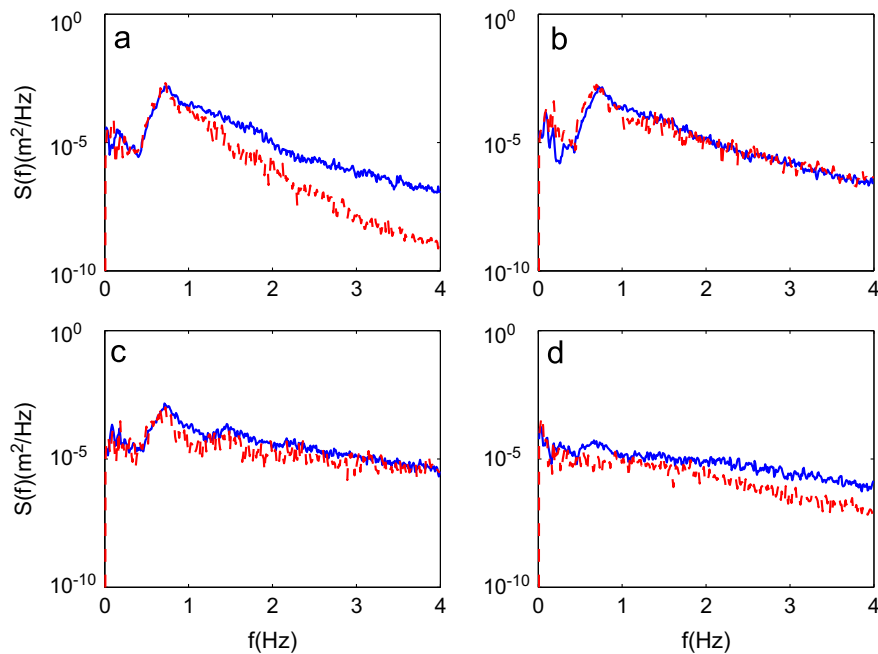


Fig. 3. Comparisons of simulated (dashed lines) and measured (solid lines) wave spectra at (a) gauge 4, (b) gauge 6, (c) gauge 8 and (d) gauge 11 for case 1 (incident wave conditions: $H_{mo}=0.0749$ m, $T_p=1.41$ s, $h=0.439$ m).

Fig. 5 demonstrates the model-data comparisons of cross-shore distributions of significant wave height, wave setup as well as the wave skewness for the second test run with incident irregular waves of $H_s=0.1567$ m, $T_p=1.84$ s and water depth of $h=0.490$ m, representative of a high wave level condition. The wave skewness is an important indicator of nonlinear wave behavior, and can be calculated as

$$\text{Skewness} = \frac{\langle \eta^3 \rangle}{\langle \eta^2 \rangle^{3/2}} \quad (29)$$

where $\langle \cdot \rangle$ is the averaging operator. Similar to the previous case, the cross-shore variations of significant wave height and wave setup are well simulated by the model. The model skill of predicting wave height is 0.954. The simulated wave skewness also agrees well with the measurement. The maximum wave skewness can be found in the outer reef flat. The comparisons of simulated and measured wave spectra at gauges 4, 6, 8 and 11 for this test run are shown in **Fig. 6**. In the deep water, the wave energy density at high frequency band is underpredicted, similar to that in the previous case. At all other wave gauges, the wave spectra are well simulated by the model, which is capable of capturing the wave spectrum evolution from offshore to the shallow reef flat.

4.2. UM experiments

The UM experiments were conducted in a two-dimensional wind wave flume with an idealized fringing reef. The flume is 35 m long, 0.7 m wide and 1.6 m high. The reef cross section consisted of a 1:12 beach followed by a 4.8-m-wide reef flat and a composite-slope reef slope as shown in **Fig. 7**. The reef surface was built using polyvinyl chloride plastic, a relatively smooth and impervious material (Nwogu and Demirbilek, 2010). Irregular waves were generated in the tank with a plunger-type wavemaker. Tests were run for a wide variety of irregular wave conditions with significant wave heights varying from 3 to 8.5 cm, spectral peak periods from 1 to 2.5 s, and water depth h_r from 0 to 5 cm on reef flat. Time histories of the water surface elevation were synthesized from JONSWAP spectral shapes with peak enhancement factor $\gamma=3.3$ using random phase method.

The computational domain is slightly shorter than the flume in the experiments. The domain length is 17.6 m, discretized by 880 grids with $\Delta x=0.02$ m. Three layers are used in the vertical direction. The test run we select has the incident wave conditions

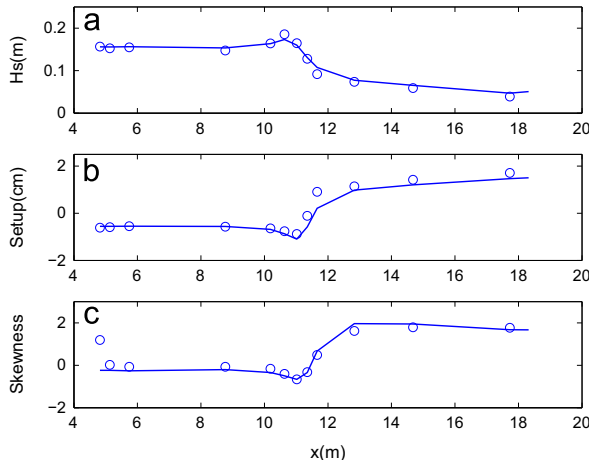


Fig. 5. Model-data comparisons of cross-shore distributions of (a) spectral significant wave height, (b) wave setup as well as (c) skewness for case 2 (incident wave conditions: $H_{mo}=0.1567$ m, $T_p=1.84$ s, $h=0.490$ m). Solid lines: simulations; circles: measurements.

of significant wave height of $H_s=0.075$ m, spectral peak wave period of $T_p=1.5$ s and water depth $h_r=3.1$ cm in the reef flat. The model results are recorded at nine wave gauges shown in **Fig. 7**. The locations of the wave gauges are $x=-1.11, -0.92, -0.59, 2.75, 3.68, 4.22, 4.80$, and 9.14 m from the toe of the reef (Nwogu and Demirbilek, 2010). Since the reef surface is relatively smooth in this experiment, we used a relatively smaller drag coefficient $C_f=0.05$ in the simulation.

The model-data comparisons of cross-shore distributions of significant wave height, infragravity wave height, wave setup as well as wave skewness are shown in **Fig. 8**. Similar to the ERDC experiments, the wave breaking occurs at the reef edge, which is well captured by the model. The energy dissipation during wave breaking is simulated by the model, resulting in fairly good model-data comparison of wave height in the reef flat. The model skill is 0.929. The simulated infragravity wave height is slightly higher than the measurement in the reef slope, while it is well predicted in the reef flat. The wave set-down and setup are well predicted by the model as well, except that the wave setup in the inner reef flat is slightly overestimated. The wave skewness in the outer flat is underestimated by the model with unclear reasons. Generally, the agreement between the measurements and simulations is good.

Fig. 9 compares the simulated and measured wave energy spectrum at gauges 2, 4, 7 and 8. As seen in **Fig. 7**, gauge 2 is located in the offshore, gauge 4 is in the reef slope, while gauges 7 and 8 are situated at the reef edge and the middle reef flat, respectively. Although the reef slope is more complicated than that in the ERDC experiments, the evolution of wave energy spectrum from offshore to the reef flat involving the generation of low-frequency waves is well captured by the model. The energy density at high frequency band ($f \geq 1.0$ Hz) is still slightly underpredicted in the deep-water wave gauges. Considering the relatively low wave energy at this frequency band, this estimation would not affect the wave height distribution significantly. In the reef slope and the reef edge, the wave spectra are well simulated by the model. From these two benchmarks, we can conclude that the shock-capturing non-hydrostatic is capable of simulating nonlinear wave processes in the reef environments with steep forereef slopes.

5. Application to a field-scale fringing reef in the Taiping Island

In the previous section, we have shown that the model is capable of simulating wave processes such as wave breaking, wave transformation as well as infragravity wave generation in the fringing reefs. In this section, we apply the model to study the infragravity waves in a field-scale fringing reef in the Taiping Island, South China Sea.

Taiping Island is located in the northern portion of the Spratly Islands in the South China Sea ($10^{\circ}23' N$, $114^{\circ}22' E$) and is the largest island in the region, with a land area of approximately 0.44 km 2 . It is elongated in an ENE–WSW direction, with a length of 1.35 km and a width of 0.4 km, on an ENE–WSW-oriented reef platform. The island is an inhabited, vegetated, low-lying sand cay encircling a narrow beach roughly 20 m wide. Fringing reefs surround the island, with reef flats extending from the toe of the beach to the reef edge for approximately 250 m to the north, 150 m to the south, and 500 m to the east and west (**Fig. 10**). A recent survey of coral reefs around the island conducted in June 2009 (Shao and Song, 2010) found that the western island has a low live coral coverage with unknown reasons. Therefore, we particularly examine the effects of coral degradation on the infragravity wave processes in this section. Two numerical experiments are conducted to achieve this objective.

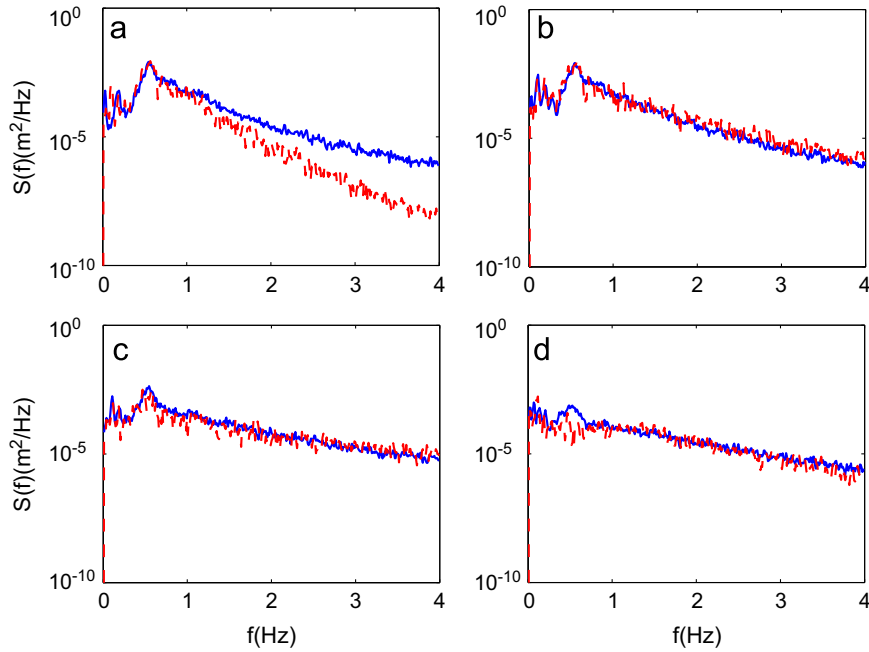


Fig. 6. Comparisons of simulated (dashed lines) and measured (solid lines) wave spectra at (a) gauge 4, (b) gauge 6, (c) gauge 9 and (d) gauge 11 for case 2 (Incident wave conditions: \$H_{mo}=0.1567 \text{ m}\$, \$T_p=1.84 \text{ s}\$, \$h=0.490 \text{ m}\$).

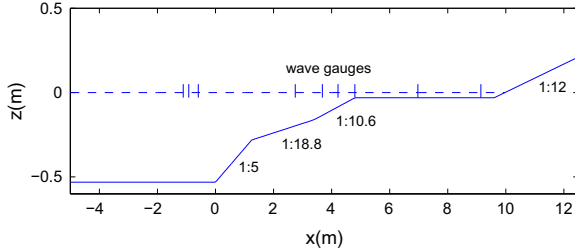


Fig. 7. The computational domain and reef topography for the flume experiment at the University of Michigan (UM). The solid lines demonstrate the locations of 9 wave gauges (gauge 1 to gauge 9 from left to right). The water depth at the reef flat is \$h_r=3.1 \text{ cm}\$.

The wave measurements around the island are limited. A wave buoy deployed in a water depth of 50 m off the southwestern coast of the island indicated that the dominant wave direction during the southwest monsoon is in WSW (Fig. 11). The significant wave height varies from 0.2 to 2.1 m and peak wave period ranges from 2.0 to 9.2 s. To study the wave processes and infragravity waves in the western reef platform, we chose a study section marked by the red solid line in the upper panel of Fig. 10. The bathymetry across this section is demonstrated in the lower panel of Fig. 10. We can see that this section consisted of a deep-water region, a reef slope and a reef flat with the width approximately 500 m. The orientation of the section is in WSW direction, consistent with the dominant wave direction. In the simulation, the section is discretized by 1200 grids with \$\Delta x = 1.0 \text{ m}\$. We choose a storm condition for incident waves. The significant wave height is \$H_s=1.8 \text{ m}\$ and the peak wave period is \$T_p=8.0 \text{ s}\$. The incident wave spectrum is the JONSWAP spectrum with peak enhancement factor \$\gamma=3.3\$. The reef-induced drag coefficient is set to be \$C_f=0.1\$ in the numerical experiment with reefs and \$C_f=0.0\$ in the numerical experiment without reefs, which indicates zero live coral coverage in the study section.

Fig. 12 shows the instantaneous surface elevations at \$x=400 \text{ m}\$, \$600 \text{ m}\$, \$800 \text{ m}\$ and \$1000 \text{ m}\$. We can clearly see the transformation of high-frequency waves to low-frequency waves as the waves propagate from offshore to the reef flat. The dashed-lines in panels

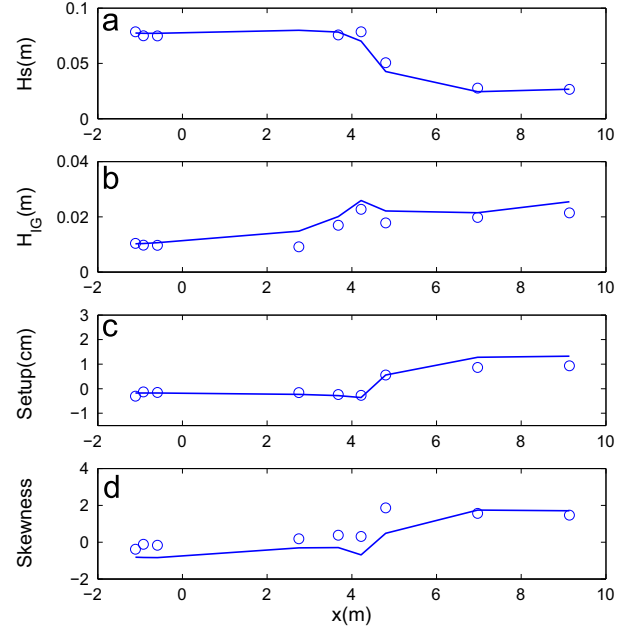


Fig. 8. Model-data comparisons of cross-shore distributions of (a) spectral significant wave height, (b) infragravity wave height, (c) wave setup and (d) skewness for the UM experiment (incident wave conditions: \$H_s=7.5 \text{ cm}\$, \$T_p=1.5 \text{ s}\$, \$h_r=3.1 \text{ cm}\$). Solid lines: simulations; circles: measurements.

(c) and (d) are obtained by using a low-pass filter, indicating the mean water level fluctuation. The fluctuation period is about 1000 s. This fluctuation possibly corresponds to the first reef oscillation mode (\$n=1\$) with a wavelength approximately equal to four times the width of the reef flat if the reef-beach system is considered to be an open basin with natural periods given by (Nwogu and Demirbilek, 2010)

$$T_n = \frac{4l_r}{(2n-1)\sqrt{gh_r}}, \quad n = 1, 2, 3, \dots \quad (30)$$

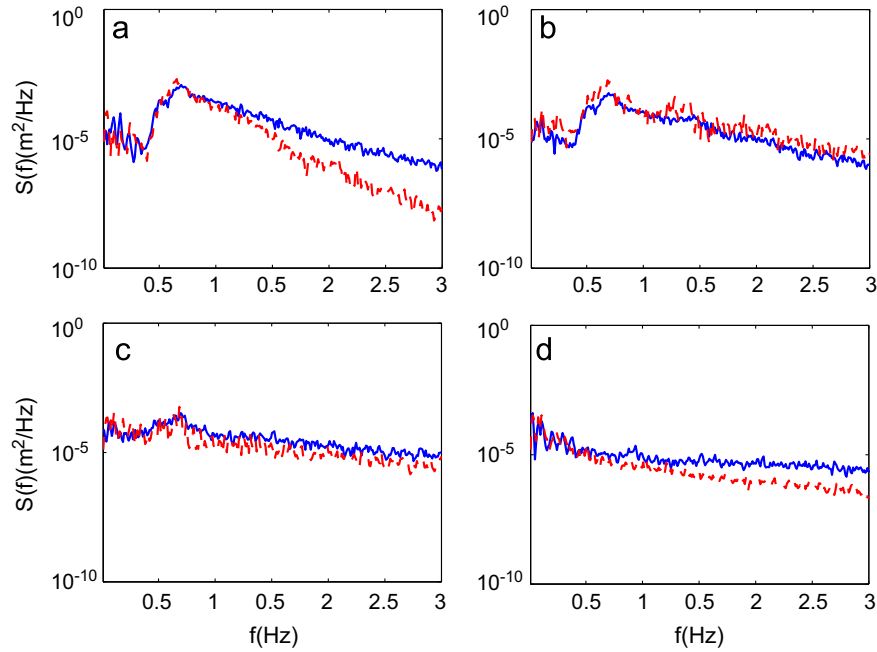


Fig. 9. Comparisons of simulated (dashed lines) and measured (solid lines) wave spectra at (a) gauge 2, (b) gauge 4, (c) gauge 7 and (d) gauge 8 for the UM experiment (incident wave conditions: $H_s=7.5 \text{ m}$, $T_p=1.5 \text{ s}$, $h_r=3.1 \text{ cm}$).

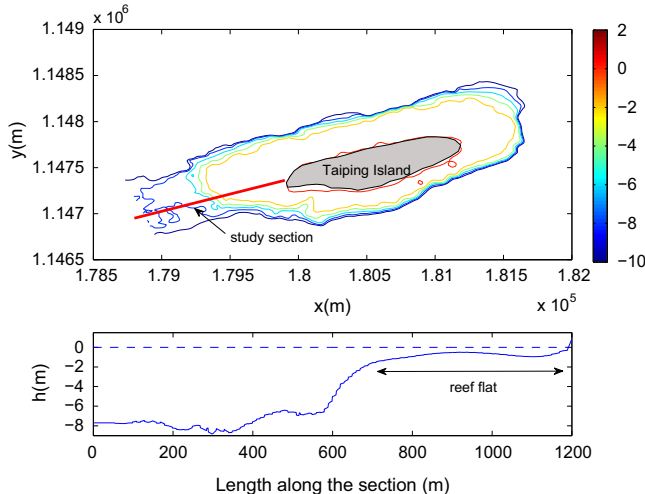


Fig. 10. Upper panel: the Taiping Island and bathymetry. The red solid line indicates the study section on the western reef flat. Lower panel: cross-shore variation of water depth along the study section. The colorbar shows the water depth in meters. (For interpretation of the references to color in this figure caption, the reader is referred to the web version of this paper.)

where $l_r \approx 500 \text{ m}$ is the width of the reef flat and $h_r \approx 0.5 \text{ m}$ is the water depth at the reef flat. The calculated natural period of the reef flat is $T_n \approx 900 \text{ s}$, which is close to the oscillation period observed from Fig. 11(c) and (d).

Fig. 13 shows the simulated cross-shore distributions of significant wave height, wave setup and skewness with and without reefs. The significant wave height is again calculated by using the Rayleigh wave height distribution. As we can see, the waves break around $x=620 \text{ m}$, which is located at the reef edge. The maximum wave set-down is also found in this location. Due to wave breaking and bottom friction, the waves lose their energy dramatically in the reef flat. The maximum wave setup is found at the outer reef flat (approximately $x=800 \text{ m}$), generating an onshore pressure gradient. The effects of coral reefs can be found on the wave height

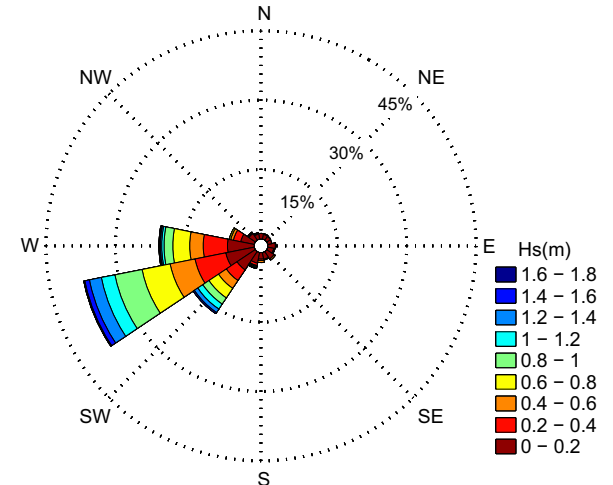


Fig. 11. The wave rose during the Southwest Monsoon in summer (May–September) based on offshore wave measurement from August 2004 to July 2005.

as well as wave skewness distributions in the reef flat. With coral degradation, the wave height in the reef flat would be significantly increased. Larger waves are expected to attack the shore. Meanwhile, the wave skewness would decrease in the outer reef flat and increase in the inner reef flat. The waves reaching the shoreline would be more nonlinear.

The wave spectra at $x=400 \text{ m}$, 600 m , 800 m and 1000 m are shown in Fig. 14. Similar to what have been found in the ERDC and UM laboratory experiments, the wave spectrum evolution from offshore to the reef flat involves cross-spectral energy transfer from the high-frequency band to the low-frequency band. At the reef flat ((c) and (d)), the wave spectra are dominated by infragravity oscillations with low-frequency $f < 0.05 \text{ Hz}$ as the wave energy in the gravity wave band ($f > 0.05 \text{ Hz}$) is mostly dissipated by wave breaking and reef-induced friction (drag). This is more clearly demonstrated in Fig. 15, which displays the cross-shore variations of gravity wave height and infragravity wave height

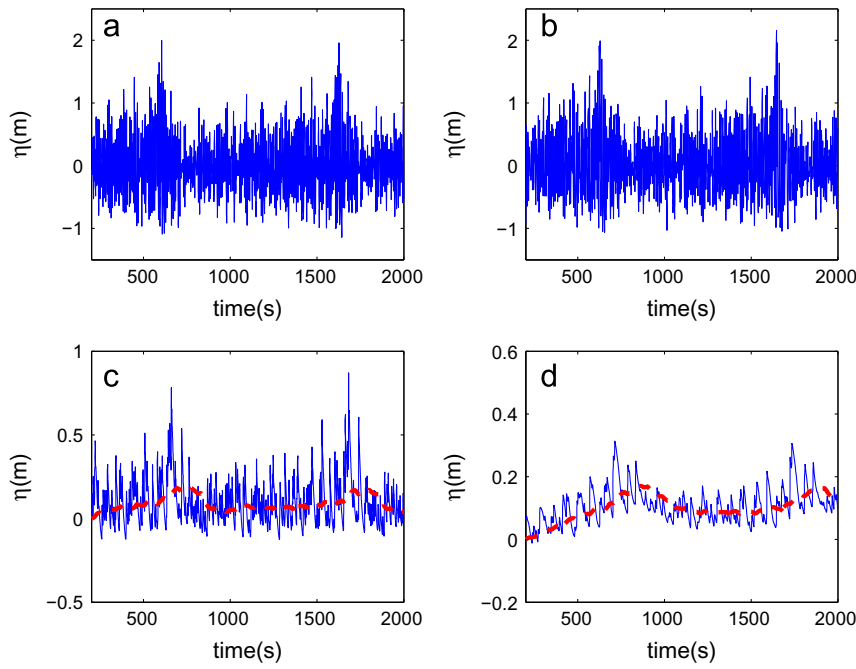


Fig. 12. The simulated free surface variations at (a) $x=400$ m; (b) $x=600$ m; (c) $x=800$ m and (d) $x=1000$ m. The dashed lines show the mean water level fluctuation obtained by using a low-pass filter. The oscillation period is approximately 1000 s.

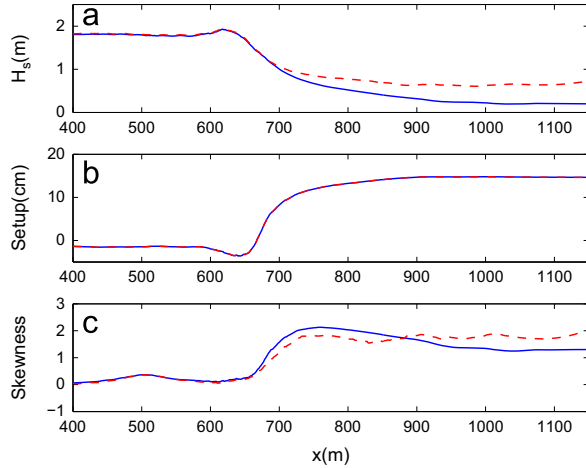


Fig. 13. The simulated cross-shore distributions of significant wave height, wave setup and wave skewness with reefs ($C_f=0.1$, solid lines) and without reefs ($C_f=0.0$, dashed lines).

obtained as

$$H_{mo,gw} = 4 \sqrt{\int_{f_c = 0.05}^{\infty} S(f) df} \quad (31)$$

and

$$H_{mo,ig} = 4 \sqrt{\int_0^{f_c = 0.05} S(f) df} \quad (32)$$

As we can see, the gravity wave height has the maximum value before wave breaking. After wave breaking, the gravity wave energy is mostly dissipated, resulting in small gravity wave height at the reef flat. The maximum infragravity wave height also reaches its maximum value at breaking point (reef edge). At the reef flat, the infragravity wave energy is dissipated by reef-induced

friction (drag). In the inner reef flat, the infragravity wave height is larger than the gravity wave height, indicating that most of wave energy is in the infragravity modes.

The coral reef effects on wave spectrum evolution and gravity/infragravity wave height distributions are also demonstrated in Figs. 14 and 15. The coral degradation would have negligible effects on the wave spectra in the offshore region and the reef slope. However, it can greatly increase the energy density over all frequency bands in the reef flat. As a consequence, the coral degradation has no impact on the gravity waves in the offshore. The increase of the wave energy in gravity wave band at the reef flat is not significant with the coral degradation, which plays a more significant role in infragravity wave motions. The coral degradation would increase the infragravity wave height not only at the reef flat, but also in the offshore. At the reef flat, most of the infragravity wave energy is dissipated by reef drag instead of wave breaking in the presence of coral reefs. With $C_f=0.1$, the coral reefs may dissipate approximately 90% of infragravity wave energy in the inner part of the 500-m-wide reef flat.

The effects of coral degradation on energy density distribution are shown in Fig. 16. In the gravity wave band, the energy density is not significantly affected by the coral degradation, except that the energy density in the inner reef flat would be slightly increased. The energy density in the gravity wave band is reduced dramatically by wave breaking at the reef edge, accompanied by the increase of spectral density in the infragravity wave band, centered at the frequency of 0.01–0.02 Hz. The coral degradation would significantly change the infragravity wave field in the reef flat. First of all, the coral degradation increases the infragravity wave energy in the inner reef flat. Without reefs, the maximum infragravity wave energy is found near the shoreline. With reefs, it is located near the reef edge. Secondly, the coral degradation would cause the energy transfer to the lower frequency waves, generating longer-period waves. In panel (b) of Fig. 16, we can see that the infragravity wave energy density in the inner flat is centered at the frequency of 0.006 Hz, which is much smaller than that at the reef edge.

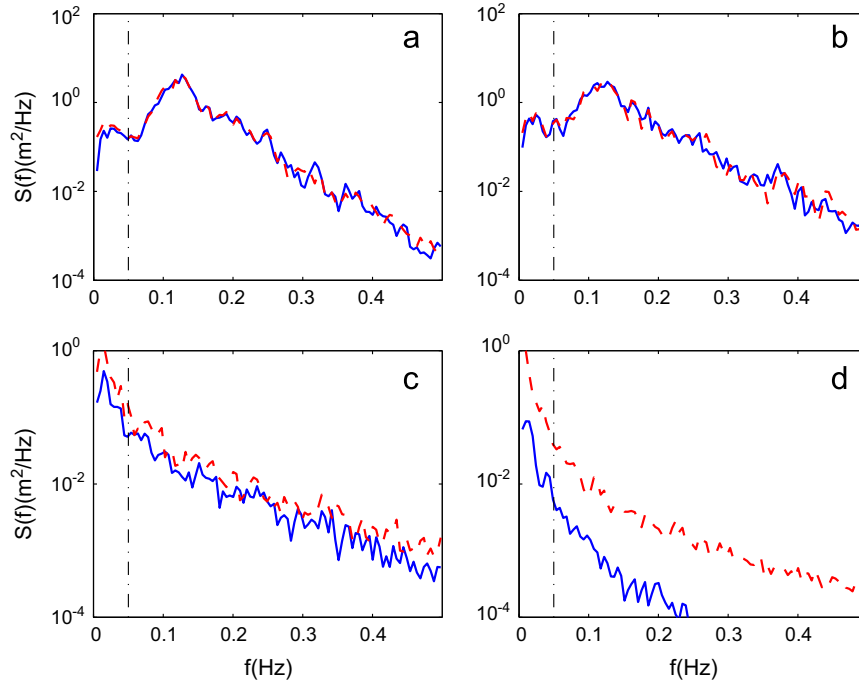


Fig. 14. The simulated energy density spectra at (a) $x=400$ m; (b) $x=600$ m; (c) $x=800$ m and (d) $x=1000$ m with reefs ($C_f=0.1$, solid lines) and without reefs ($C_f=0.0$, dashed lines). The dash-dotted lines demarcate the gravity and infragravity wave ($f < -0.05$ Hz) bands.

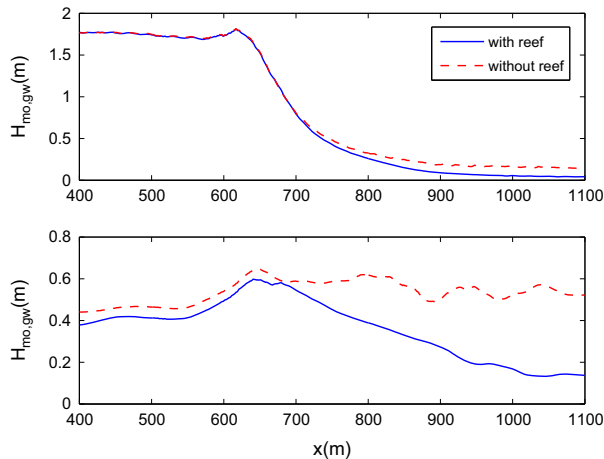


Fig. 15. Upper panel: cross-shore variation of wave energy in gravity wave band ($f > 0.05$ Hz); Lower panel: cross-shore variation of wave energy in infragravity wave band ($f \leq 0.05$ Hz). Solid lines: with reefs ($C_f=0.1$); Dashed lines: no reefs ($C_f=0.0$).

6. Conclusions

In this paper, a shock-capturing non-hydrostatic model was developed to study infragravity waves in the fringing reefs. The reef effects on the water column were considered by introducing a drag force in the momentum equations. The shock-capturing HLL scheme was used to solve the governing equations, and was proved to be capable of capturing wave breaking and broken wave propagation in the surf zone. The model was applied to reproduce the measurements in the two sets of laboratory experiments: ERDC experiments and UM experiments. Numerical results showed that the model could well simulate wave transformation, wave breaking, wave spectrum evolution as well as infragravity waves in the coral reefs.

The model was also utilized to examine the effects of coral degradation on infragravity waves in the western reef platform in

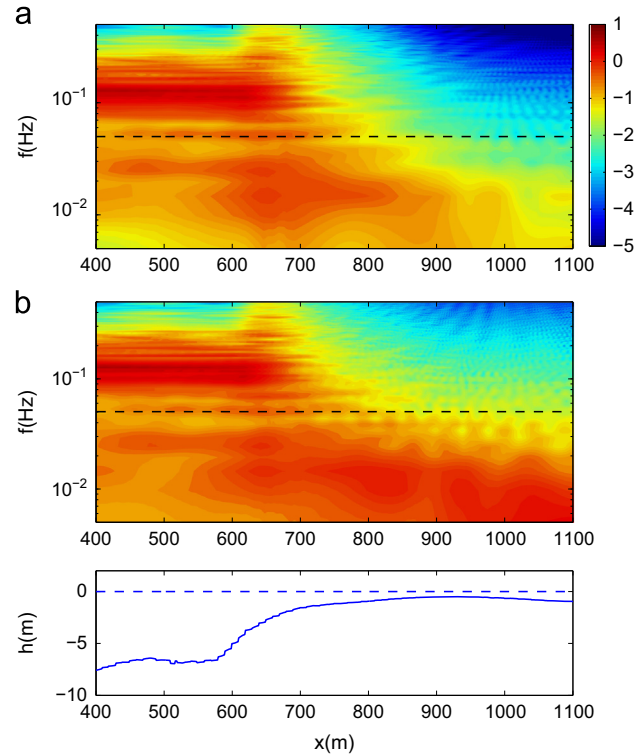


Fig. 16. Comparison of simulated cross-shore distributions of spectral density with reefs (panel (a)) and without reefs (panel (b)).

the Taiping Island, South China Sea. Model results confirmed the existence of infragravity waves in this region, which are possibly related to the fundamental mode of resonance of reef flat. At the reef flat, the wave energy in the gravity wave band is mostly dissipated by wave breaking, while the infragravity wave energy is mostly dissipated by reef-induced friction. The coral degradation has significant effects on infragravity wave motions, which would

become more energetic at the reef flat. It would also lead to the energy transfer to lower frequency waves, generating longer-period waves. It has been demonstrated in the paper that the non-hydrostatic model would be a highly useful tool for studying wave processes in reef environments.

Acknowledgments

Ma acknowledges the financial support of National Science Foundation (OCE-1334641) and Old Dominion University Research Foundation (Multidisciplinary Seed Funding (MSF) Grants, Project no. 545411). Su acknowledges the support of the National Science Council of Taiwan under the Grant NSC103-XXX. Liu acknowledges the support of National Science Foundation of China (41372240). The authors are grateful to CECI Engineering Consults, Inc. for providing the valuable field data.

References

- Battjes, J.A., Bakkenes, H.J., Janssen, T.T., van Dongeren, A.R., 2004. Shoaling of subharmonic gravity waves. *J. Geophys. Res.* 109, C02009, <http://dx.doi.org/10.1029/2003JC001863>.
- Bowen, A.J., Huntley, D.A., 1984. Waves, long waves and nearshore morphology. *Mar. Geol.* 60, 1–13.
- Bradford, S.F., 2011. Nonhydrostatic model for surf zone simulation. *J. Waterway Port Coast. Ocean Eng.* 137 (4), 163–174.
- Brander, R.W., Kench, P.S., Hart, D., 2004. Spatial and temporal variations in wave characteristics across a reef platform, Warraber Island, Torres Strait, Australia. *Mar. Geol.* 207, 169–184.
- Demirbilek Z., Nwogu, O.G., Ward, D.L., 2007. Laboratory Study of Wind Effect on Runup over Fringing Reefs. Report 1: Data Report. Coastal and Hydraulics Laboratory Technical Report No. ERDC/CHL-TR-07-4, U.S. Army Engineer Research and Development Center, Vicksburg, Miss.
- Gottlieb, S., Shu, C.-W., Tadmor, E., 2001. Strong stability-preserving high-order time discretization methods. *SIAM Rev.* 43, 89–112.
- Hardy, T.A., Young, I.R., 1996. Field study of wave attenuation on an offshore coral reef. *J. Geophys. Res.* 101 (C6), 14311–14326.
- Harten, A., Lax, P., van Leer, B., 1983. On upstream differencing and Godunov-type schemes for hyperbolic conservation laws. *SIAM Rev.* 25, 35.
- Herbers, T.H.C., Elgar, S., Guza, R.T., 1994. Infragravity-frequency (0.005–0.05 Hz) motions on the shelf. Part I: forced waves. *J. Phys. Oceanogr.* 24, 917–927.
- Herbers, T.H.C., Guza, R.T., 1994. Nonlinear wave interactions and high-frequency seafloor pressure. *J. Geophys. Res.* 99, 10035–10048.
- Janssen, T.T., Battjes, J.A., van Dongeren, A.R., 2003. Long waves induced by short-wave groups over a sloping bottom. *J. Geophys. Res.* 108, <http://dx.doi.org/10.1029/2002JC001515>.
- Longuet-Higgins, M.S., Stewart, R.W., 1962. Radiation stress and mass transport in gravity waves, with application to surf beat. *J. Fluid Mech.* 13, 481–504.
- Longuet-Higgins, M.S., Stewart, R.W., 1964. Radiation stress in water waves: physical discussion with applications. *Deep Sea Res.* 11, 529–562.
- Lowe, R.J., Falter, J.L., Bandet, M.D., Pawlak, G., Atkinson, M.J., Monismith, S.G., Koseff, J.R., 2005. Spectral wave dissipation over a barrier reef. *J. Geophys. Res.* 110 (C4), C04001, <http://dx.doi.org/10.1029/2004JC002711>.
- Lowe, R.J., Falter, J.L., Monismith, S.G., Atkinson, M.J., 2009. Wave-driven circulation of a coastal reef-lagoon system. *J. Phys. Oceanogr.* 39, 873–893.
- Lugo-Fernández, A., Roberts, H.H., Wiseman Jr, W.J., Carter, B.L., 1998. Water level and currents of tidal and infragravity periods at Tague Reef, St. Croix (USVI). *Coral Reefs* 17, 343–349.
- Ma, G., Shi, F., Kirby, J.T., 2012. Shock-capturing non-hydrostatic model for fully dispersive surface wave processes. *Ocean Model.* 43–44, 22–35.
- Ma, G., Kirby, J.T., Shi, F., 2013a. Numerical simulation of tsunami waves generated by deformable submarine landslides. *Ocean Model.* 69, 146–165.
- Ma, G., Kirby, J.T., Su, S., Figlus, J., Shi, F., 2013b. Numerical study of turbulence and wave damping induced by vegetation canopies. *Coast. Eng.* 80, 68–78.
- Massel, S.R., Gourlay, M.R., 2000. On the modelling of wave breaking and set-up on coral reefs. *Coast. Eng.* 39, 1–27.
- Munk, W.H., Sargent, M.C., 1948. Adjustment of Bijini Atoll to ocean waves. *Trans. Am. Geophys. Union* 29, 855–860.
- Nakaza, E., Hino, M., 1991. Bore-like surf beat in a reef zone caused by wave groups of incident short period waves. *Fluid Dyn. Res.* 7, 89–100.
- Nwogu, O., Demirbilek, Z., 2010. Infragravity wave motions and runup over shallow fringing reefs. *J. Waterway Port Coast. Ocean Eng.* 136, 295–305.
- Péquignet, A.C.N., Becker, J.M., Merrifield, M.A., Aucan, J., 2009. Forcing of resonant modes on a fringing reef during tropical storm Man-Yi. *Geophys. Res. Lett.* 36, L03607, <http://dx.doi.org/10.1029/2008GL036259>.
- Pomeroy, A., Lowe, R., Symonds, G., Van Dongeren, A., Moore, C., 2012. The dynamics of infragravity wave transformation over a fringing reef. *J. Geophys. Res.* 117, C11022, <http://dx.doi.org/10.1029/2012JC008310>.
- Reniers, A.J.H.M., MacMahan, J.H., Thornton, E.B., Stanton, T.P., 2006. Modelling infragravity motions on a rip-channel beach. *Coast. Eng.* 53, 209–222.
- Rijnsdorp, D.P., Smit, P.B., Zijlema, M., 2014. Non-hydrostatic modelling of infragravity waves under laboratory conditions. *Coast. Eng.* 85, 30–42.
- Roeber, V., Cheung, K.F., 2012. Boussinesq-type model for energetic breaking waves in fringing reef environments. *Coast. Eng.* 70, 1–20.
- Rosman, J.H., Hench, J.L., 2011. A framework for understanding drag parameterizations for coral reefs. *J. Geophys. Res.* 116, C08025, <http://dx.doi.org/10.1029/2010JC006892>.
- Shao, K.-T., Song, Y.-H., 2010. Assessment of the Feasibility of Establishing Taiping Island as a Marine National Park. Construction and Planning Agency, Ministry of Interior, Taiwan (in Chinese).
- Sheremet, A., Kaihatu, J.M., Su, S.-F., Smith, E.R., Smith, J.M., 2011. Modeling of nonlinear wave propagation over fringing reefs. *Coast. Eng.* 58, 1125–1137.
- Smit, P., Zijlema, M., Stelling, G.S., 2013. Depth-induced wave breaking in a non-hydrostatic, near-shore wave model. *Coast. Eng.* 76, 1–16.
- Smit, P., Janssen, T., Holthuijsen, L., Smith, J., 2014. Non-hydrostatic modeling of surf zone wave dynamics. *Coast. Eng.* 83, 36–48.
- Symonds, G., Huntley, D., Bowen, A., 1982. Two dimensional surf-beat: Long wave generation by a time-varying break point. *J. Geophys. Res.* 87, 492–498.
- Van Dongeren, A., Lowe, R., Pomeroy, A., Trang, D.M., Roelvink, D., Symonds, G., Ranasinghe, R., 2013. Numerical modeling of low-frequency wave dynamics over a fringing coral reef. *Coast. Eng.* 73, 178–190.
- Young, I.R., 1989. Wave transformation over coral reefs. *J. Geophys. Res.* 94, 9779–9789.
- Zhou, J.G., Gauson, D.M., Mingham, C.G., Ingram, D.M., 2001. The surface gradient method for the treatment of source terms in the shallow-water equations. *J. Comput. Phys.* 168, 1–25.
- Zijlema, M., Stelling, G.S., 2008. Efficient computation of surf zone waves using the nonlinear shallow water equations with non-hydrostatic pressure. *Coast. Eng.* 55, 780–790.